Tailoring Solution-Processable Li Argyrodites $Li_{6+x}P_{1−x}M_xS_5I$ (M = Ge, Sn) and Their Microstructural Evolution Revealed by Cryo-TEM for All-Solid-State Batteries

Yong Bae Song, Dong Hyeon Kim, Hiram Kwak, Daseul Han, Sujin Kang, Jong Hoon Lee, Seong-Min Bak, Kyung-Wan Nam, Hyun-Wook Lee,* and Yoon Seok Jung*

ABSTRACT: Owing to their high Li^+ conductivities, mechanical sinterability, and solution processability, sulfide Li argyrodites have attracted much attention as enablers in the development of high-performance all-solid-state batteries with practicability. However, solution-processable Li argyrodites have been developed only for a composition of Li_6PS_5X (X = Cl, Br, I) with insufficiently high Li^+ conductivities ($\sim 10^{-4}$ S cm^{-1}). Herein, we report the highest Li^+ conductivity of 0.54 mS cm^{-1} at 30 °C ($Li_{6.5}P_{0.5}Ge_{0.5}S_5I$) for solution-processable iodine-based Li argyrodites. A comparative investigation of three iodine-based argyrodites of unsubstituted and Ge- and Sn-substituted solution-processed Li_6PS_5I with varied heat-treatment temperature elucidates the effect of microstructural evolution on Li^+ conductivity. Notably, local nanostructures consisting of argyrodite nanocrystallites in solution-processed $Li_{6.5}P_{0.5}Ge_{0.5}S_5I$ have been directly captured by cryogenic transmission electron microscopy, which is a first for sulfide solid electrolyte materials. Specifically, the promising electrochemical performances of all-solid-state batteries at 30 °C employing $LiCoO_2$ electrodes tailored by the infiltration of $Li_{6.5}P_{0.5}Ge_{0.5}S_5I$−ethanol solutions are successfully demonstrated.

KEYWORDS: Solid-state batteries, solid electrolytes, cryo-TEM, sulfides, solution process
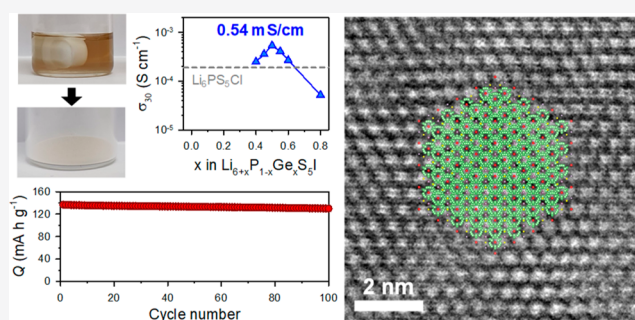
Inorganic Li^+ superionic conductors have gained extensive attention as a promising alternative to flammable organic liquid electrolytes used in conventional lithium ion batteries (LIBs).[1−8] In particular, extremely high ionic conductivities reaching a maximum value of $\sim 10^{-2}$ S cm^{-1} at room temperature (e.g., $Li_{9.54}Si_{1.74}P_{1.44}S_{11.7}Cl_{0.3}$:[2] 25.3 mS cm^{-1}) and good deformability that enables mechanical sintering strongly suggest the significant potential of sulfide solid electrolyte (SE) materials for achieving high-performance all-solid-state Li or Li ion batteries (ASLBs) to scale.[2,4,9,10] Argyrodite SEs represented by Li_6PS_5X (X = Cl, Br, I) show high Li^+ conductivities in the range of $10^{-3}–10^{-2}$ S cm^{-1} at room temperature and possess a stable face-centered-cubic crystal structure indicating high thermal and electrochemical stabilities.[11−14]

Recent extensive investigations on theoretical and experimental studies for Li-argyrodites have achieved notable progress.[9,13−17] Consistent with a prediction by density functional theory molecular dynamics simulations,[13] an increase in halogen and the corresponding increase in Li significantly enhanced Li^+ conductivities that reach 10^{-2} S cm^{-1} ($Li_{5.5}PS_{4.5}Cl_{1.5}$).[18] Zeier and co-workers revealed that the much lower Li^+ conductivity of an iodine-based argyrodite, Li_6PS_5I, as compared with that of bromine- or chlorine-based

argyrodites, Li_6PS_5Br or Li_6PS_5Cl, despite larger and more polarizable lattices, could be associated with the restricted anion-site disorder between free S^{2-} and I^-.[11,14] Notably, the same group recently demonstrated that the aliovalent substitution of P^{5+} with larger ions, such as Ge^{4+}, Si^{4+}, and Sn^{4+}, could induce the anion-site disorder and result in high ionic conductivities ($Li_{6.6}P_{0.4}Ge_{0.6}S_5I$,[15] 5.4 mS cm^{-1}; $Li_{6.3}P_{0.7}Sn_{0.3}S_5I$,[19] 0.1 mS cm^{-1}; and $Li_{6.7}P_{0.3}Si_{0.7}S_5I$,[19] 2.0 mS cm^{-1}), thereby opening up new opportunities. Furthermore, Nazar and co-workers extended the exploration of new iodine-based argyrodites by the isovalent substitution of P^{5+} with Sb^{5+} and identified $Li_{6.6}Si_{0.6}Sb_{0.4}S_5I$ (14.8 mS cm^{-1}).[9]

A unique functionality of Li argyrodites is the solution processability using anhydrous ethanol (EtOH).[4,20−23] Our group demonstrated that several SE materials (e.g., Li_4SnS_4, $LiI–Li_4SnS_4$, Li_6PS_5Cl, Na_3SbS_4, $Na_{4−x}Sn_{1−x}Sb_xS_4$, and
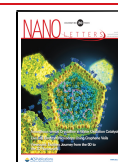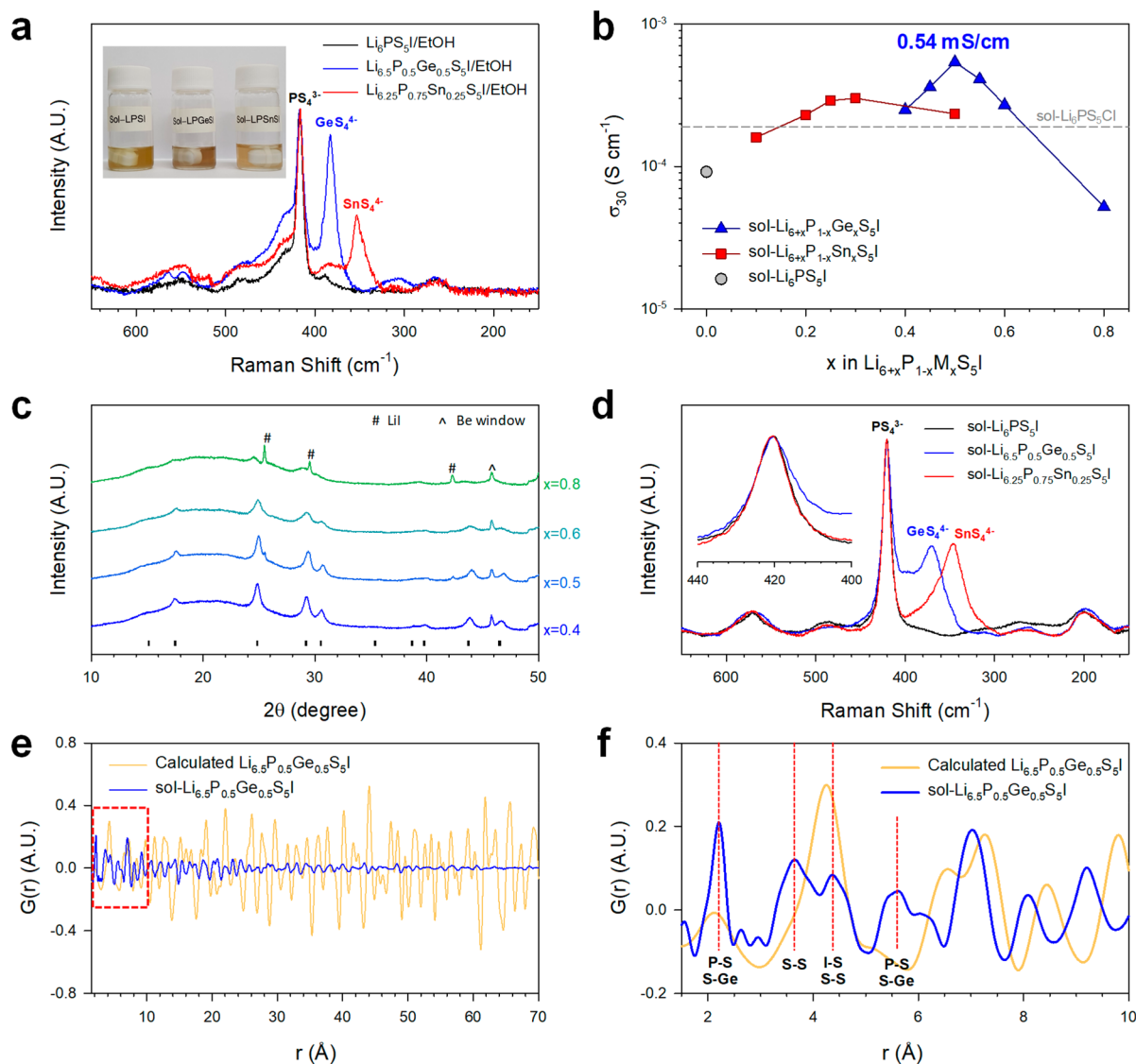
Figure 1. Characterization of solution-processed $Li_{6+x}P_{1-x}M_xS_5I$ (LPMSI, M = Ge, Sn). (a) Raman spectra and photographs of homogeneous solutions of LPMSI dissolved in anhydrous EtOH. (b) Li^+ conductivities at 30 °C for sol-LPMSI as a function of x in $Li_{6+x}P_{1-x}M_xS_5I$. The conductivity for sol-L_6PS_5Cl is also shown for comparison. (c) XRD patterns of sol-LPGeSI. Bragg positions for Li_6PS_5I (ICSD no. 418489) are also shown at the bottom. (d) Raman spectra for sol-LPMSI heat treated at 180 °C, indicating signatures for polyanions. PDF G(r) for sol-$Li_{6.5}P_{0.5}Ge_{0.5}S_5I$ heat treated at 180 °C in comparison with the PDF for the calculated $Li_{6.5}P_{0.5}Ge_{0.5}S_5I$ using the bulk crystalline model structure taken from ref 15 in the r ranges of (e) 1.5 to 70 Å and (f) 1.5 to 10 Å.

$Na_4(B_{12}H_{12})(B_{10}H_{10}))$ could be fully dissolved in selected solvents, such as methanol, EtOH, and water, without the occurrence of a side reaction, forming homogeneous solutions, and could be recovered via the elimination of the solvents (and subsequent heat treatment).[4,22,24−29] The homogeneous SE solutions could be used for direct SE coatings on active materials or the infiltration of slurry-cast porous electrodes used in conventional LIBs.[22,28−30] In both cases, the good wetting property of SE solutions enabled intimate ionic contacts with active materials and thereby enhanced the electrochemical performance of all-solid-state batteries significantly. To date, the solution processes for Li-argyrodites have been developed only for a composition of Li_6PS_5X (X = Cl, Br, I) (Table S1).[4,20−22] Unfortunately, Li^+ conductivity of the solution-processed Li_6PS_5Cl was insufficiently high (maximum value ~10^{-4} S cm^{-1}) under heat treatment at a low temperature of ≤200 °C, which was necessary for

applications of SE coatings or infiltration and responsible for low crystallinity.

Low-crystalline SE materials including such solution-processed Li-argyrodites and mechanical-milling-derived samples (e.g., glasses and glass-ceramics) are important for ASLBs.[20,31−37] It was suggested that inconsistencies in the reported values of Li^+ conductivities for Li−P−S glass-ceramics (e.g., Li_3PS_4) were associated with complex local phase evolution, which varied with synthesis conditions and precursors.[38] Transmission electron microscopy (TEM) analysis could be a straightforward method for disclosing the microstructures of such low crystalline materials. Unfortunately, direct capturing for sulfide SE materials via conventional TEM has been unsuccessful because of their vulnerability toward the electron beam.[39] In this regard, cryogenic TEM (cryo-TEM), which has been emerging as a powerful tool for the observation of electron-beam-sensitive
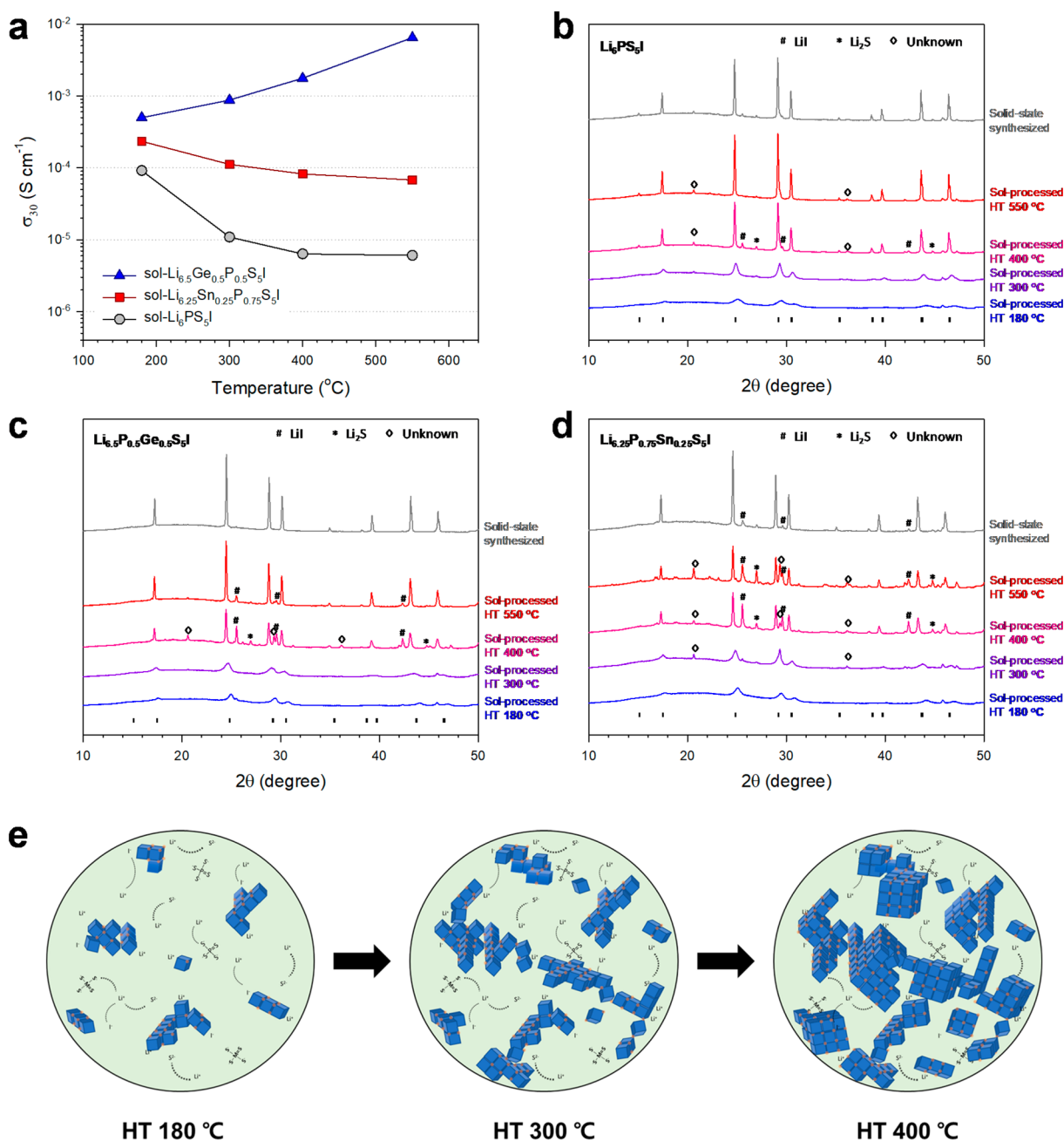
Figure 2. Results of sol-LPMSI heat treated at various temperatures. (a) Li$^+$ conductivities at 30 °C for sol-LPMSI prepared at different heat-treatment temperatures. XRD patterns for (b) sol-LPSI, (c) sol-LPGeSI, and (d) sol-LPSnSI prepared at different heat-treatment temperatures. Bragg positions for Li$_6$PS$_5$I (ICSD no. 418489) and XRD patterns for the solid-state-synthesized LPMSI samples heat-treated at 550 °C are also shown for comparison in (b−d). (e) Schematic illustrating microstructural evolution for sol-LPMSI with increasing heat-treatment temperature.

materials such as biomolecules, Li metal, and solid electrolyte interphases, could be highly promising for sulfide SE materials as well.[40−43] There have been no reports on the cryo-TEM measurement of sulfide SE materials thus far.

Herein, we develop new solution-processable iodine-based Li-argyrodites (Li$_6$PS$_5$I, Li$_{6+x}$P$_{1−x}$M$_x$S$_5$I (M = Ge, Sn)) using anhydrous EtOH as a solvent. An Li$^+$ conductivity of 0.54 mS cm$^{−1}$ at 30 °C is achieved for Li$_{6.5}$P$_{0.5}$Ge$_{0.5}$S$_5$I, and it is the highest reported value achieved among the solution-processable Li-argyrodites to date. Effects of the heat-treatment temperature and composition of iodine-based argyrodites on microstructure and Li$^+$ conductivity are systematically investigated via electrochemical impedance spectroscopy

(EIS), X-ray diffraction (XRD), Raman spectroscopy, and pair distribution function (PDF) measurements. Importantly, cryo-TEM directly captures local nanostructures for sulfide SE materials for the first time. Finally, Li$_{6.5}$P$_{0.5}$Ge$_{0.5}$S$_5$I−EtOH solution is used to infiltrate slurry-cast LiCoO$_2$ electrodes. The resulting LiCoO$_2$ in all-solid-state cells demonstrates a high reversible capacity (155 mA h g$^{−1}$ at 0.1 C) and rate capability with excellent cycling stability (94.9% capacity retention after 100 cycles at 0.2 C) at 30 °C between 3.0 and 4.3 V (vs Li/ Li$^+$), attributed to the high Li$^+$ conductivity of Li$_{6.5}$P$_{0.5}$Ge$_{0.5}$S$_5$I and intimate ionic contacts.

Iodine-based Li−P(−M)−S−I samples used for the solution process were prepared via mechanochemical milling of the

precursors (Li_2S, P_2S_5, GeS_2, SnS_2, and LiI), referred to as BM-LPMSI (M = Ge, Sn). For the solution process, the as-prepared BM-LPMSI powders were dissolved completely in anhydrous EtOH, forming homogeneous SE solutions as shown in the inset in Figure 1a. Raman spectra for the homogeneous SE solutions show signatures for PS_4^{3-} at 417 cm^{-1} (for all samples), GeS_4^{4-} at 382 cm^{-1} (for $Li_{6.5}P_{0.5}Ge_{0.5}S_5I$), and SnS_4^{4-} at 353 cm^{-1} (for $Li_{6.25}P_{0.75}Sn_{0.25}S_5I$).[24,25] Moreover, characteristic Raman peaks for EtOH remain constant, and no other impurity peaks were observed for any of the BM-LPMSI/EtOH solutions (Figure S1). These results confirm the intactness of polysulfide species in the EtOH solution (Figure 1a). The final products of SEs were crystallized by evaporating the solvent from the solutions under vacuum, followed by heat treatment at 180 °C under vacuum, and are referred to as sol-LPMSI (M = Ge, Sn). To investigate the relationship between the microstructure of solution-processed SEs and the heat-treatment temperature, further heat treatment under Ar at various temperatures was also carried out, which is discussed later.

Li$^+$ conductivities at 30 °C and the corresponding activation energies for sol-LPMSI heat treated at 180 °C were measured by an AC impedance method using Ti/SE/Ti symmetric cells, as shown in Figures 1b and S2, respectively. The highest Li$^+$ conductivities for sol-LPGeSI and sol-LPSnSI are found at $x = 0.5$ and 0.3 in $Li_{6+x}P_{1-x}M_xS_5I$, respectively. These values are higher than that for conventional sol-Li_6PS_5Cl ($\sim$0.19 mS cm^{-1}). They are also higher than that for sol-LPSI (Li_6PS_5I), possibly owing to the increased anion-site disorder and Li$^+$ concentration.[15] Notably, the maximum Li$^+$ conductivity for sol-LPGeSI achieved with sol-$Li_{6.5}P_{0.5}Ge_{0.5}S_5I$ (0.54 mS cm^{-1}) is the highest among those reported solution-processed Li-argyrodites so far.[15,19]

XRD patterns for sol-LPGeSI and Raman spectra for sol-LPMSI are shown in Figure 1c, d, respectively. (The heat-treatment temperature was 180 °C.) Broad but clear argyrodite characteristic peaks are seen in all XRD patterns. At $x = 0.8$ in $Li_{6+x}P_{1-x}Ge_xS_5I$, a highly intense peak for the LiI impurity is observed, indicating that the solid solution limit of x is far less than 0.8.[15] This is consistent with the volcano-shaped Li$^+$ conductivities centered at $x = 0.5$ in Figure 1b. In Raman spectra in Figure 1d, strong peaks at 420 cm^{-1} shown for all three samples of sol-LPSI, sol-LPGeSI, and sol-LPSnSI indicate the presence of PS_4^{3-}.[21] Moreover, the peaks centered at 370 and 345 cm^{-1} for sol-LPGeSI and sol-LPSnSI originate from GeS_4^{4-} and SnS_4^{4-}, respectively.[24,25] Furthermore, the PS_4^{3-} peak broadness in the Raman spectra, reflecting the degree of disorder,[44,45] is the largest for sol-LPGeSI.

A qualitative analysis of the PDF data for sol-LPGeSI was also carried out by comparing the calculated PDF data using the model structure of bulk crystalline LPGeSI.[15] As seen in Figure 1e, PDF data for the calculated model and sol-LPGeSI show similar interatomic structures in the short-range regime below $\sim$10 Å. However, the oscillation for sol-LPGeSI gradually decays to nearly zero at $r \approx 60$ Å, in contrast to that of the calculated bulk crystalline LPGeSI. This result implies that sol-LPGeSI has limited structural coherence within the $\sim$6 nm length scale, indicating a lack of long-range order,[46] which is in line with the broad XRD peaks in Figure 1c. Figure 1f shows a close-up of the shorter atom–atom distances (r) between 1.5 and 10 Å. The PDF peaks for sol-LPGeSI at 2.125, 3.471, 3.77, and 5.643 Å correspond to the atomic bonding for P(Ge)–S, S–S, S–S(I), and P(Ge)–S

in the argyrodite structure, verifying the formation in the short-range regime. However, there is a noticeable variation in the peak intensity as compared with that in the PDF of the calculated bulk crystalline LPGeSI, implying differences in atomic position and occupancy between sol-LPGeSI and the bulk crystalline LPGeSI in the local-structure regime. We also note that the overall shifts of peak positions to the lower r distance for sol-LPGeSI suggest a decreased lattice volume compared with that of bulk crystalline LPGeSI.

In summary, complementary analysis by the XRD, Raman spectroscopy, and PDF measurements so far confirms that the low- and/or nanocrystalline argyrodite framework structure for iodine-based LPMSI could be formed successfully via the solution process.

It is interesting that sol-LPSnSI shows higher Li$^+$ conductivity than sol-Li_6PS_5Cl (Figure 1b), despite its lower Li$^+$ conductivity in the crystalline phase. Moreover, the Li$^+$ conductivity of sol-LPSI reaches almost 10^{-4} S cm^{-1}, which is far higher than that of crystalline LPSI prepared at a high temperature of 550 °C (0.0013 mS cm^{-1}).[14] This unique feature of the solution-processed iodine-based argyrodites suggests a veiled effect of microstructure derived from the solution process.[39]

To further investigate the effect of composition and microstructure on Li$^+$ conductivity for sol-LPMSI, Li$^+$ conductivities and XRD patterns for sol-LPMSI heat treated at different temperatures (180, 300, 400, and 550 °C) were measured (Figure 2a–d). For sol-LPGeSI and sol-LPSnSI, samples with a composition showing the highest Li$^+$ conductivities were used ($x = 0.50$ and 0.25 in $Li_{6+x}P_{1-x}M_xS_5I$ for M = Ge and Sn, respectively). As the heat-treatment temperature is increased from 180 to 550 °C, distinctly opposite behaviors are observed for sol-LPGeSI and sol-LPSI (Figure 2a). Though the Li$^+$ conductivity of sol-LPSI decreases from 0.092 to 0.0061 mS cm^{-1}, that of sol-LPGeSI increases from 0.50 up to 6.5 mS cm^{-1}. As clearly shown in the XRD patterns (Figure 2b–d), the increase in the heat-treatment temperature leads to sharpened and strengthened peaks, indicating enhanced crystallinity.[37,39] The extremely different Li$^+$ conductivities between highly crystalline sol-LPGeSI and sol-LPSI heat treated at 550 °C are consistent with those highlighted in previous reports, wherein the increased S^{2-}/I^- site disorder upon Ge substitution in Li_6PS_5I renders enhanced Li$^+$ movement drastically.[15] The contrasting behavior of Li$^+$ conductivities for sol-LPSI and sol-LPSI upon varying the heat-treatment temperature could be understood by considering their microstructural evolution as follows. Solution-processed SEs heat-treated at a low temperature of 180 °C would have glass-ceramic structures in which nanocrystalline and amorphous phases coexist.[20,21,37,47] As illustrated in Figure 2e, the crystalline phase would grow as the heat-treatment temperature is increased, which is beneficial for LPGeSI but detrimental for LPSI. Thus, distinctly opposite contributions of highly crystalline LPGeSI and LPSI phases, respectively, could be responsible for the overall behavior of Li$^+$ conductivities for solution-processed Li argyrodites. Conversely, the solution process could be a promising method to enable low ion-conductive materials to be useful materials.[22,24,37]

While global structural information was analyzed by XRD, Raman spectroscopy, and PDF measurements, local nano-structural information was acquired by cryo-TEM analysis for sol-LPGeSI ($Li_{6.5}P_{0.5}Ge_{0.5}S_5I$) heat-treated at 180 °C (Figure 3). Measurement attempts by conventional TEM resulted in a
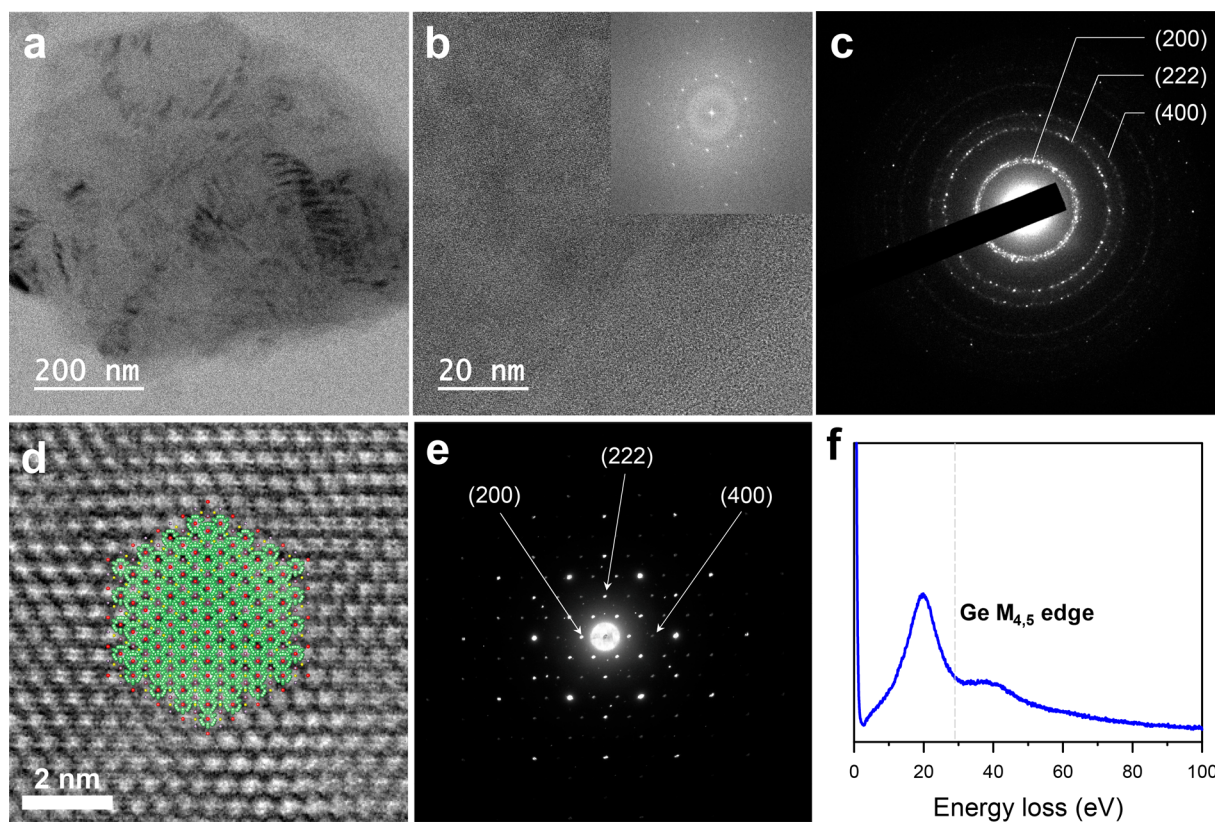
Figure 3. Cryo-TEM results for sol-LPGeSI heat treated at 180 °C. Cryo-TEM images at (a) low magnification and (b) high magnification with an inverse-FFT pattern. (c) Corresponding SAED patterns indicating polycrystallites of the argyrodite phase. (d) Magnified high-resolution cryo-TEM image revealing the cubic structure of the argyrodite phase. (e) SAED patterns indicating a single-crystallite argyrodite phase. Cryo-TEM images corresponding to (d) and (e) are provided in Supporting Information (Figure S4). (f) EELS spectrum showing the signature of Ge.

severe and immediate destruction of sulfide SE materials by the electron beam (Movie S1). Cryo-TEM measurement was conducted at cryogenic temperature (−175 °C) without any exposure to ambient air using a double-tilt cryogenic TEM holder. Prior to cryo-TEM analysis, a cryogenic XRD measurement for sol-LPGeSI was conducted at −175 °C to check any possible phase changes at cryogenic temperature. As shown in the cryogenic XRD pattern, the crystallinity and structure of sol-LPGeSI were well maintained at −175 °C, compared with the XRD pattern at 25 °C (Figure S3). The cryo-TEM image of an ∼700-nm-sized particle of sol-LPGeSI is shown in Figure 3a. The corresponding high-resolution image with fast Fourier transform (FFT) patterns and selected area electron diffraction (SAED) patterns are shown in Figure 3b, c, respectively. Multiple spots in the SAED patterns in Figure 3c indicate a polycrystalline feature of argyrodite nanocrystals for solution-derived LPGeSI. Consistent results were obtained in other magnified images (Figure S4). In particular, a high-resolution lattice image on the atomic scale is successfully acquired, as shown in Figure 3d, reflecting the argyrodite cubic structure with [111]-directed alignment (Figure S5). The SAED patterns in Figure 3e perfectly match the argyrodite crystal (space group $F\bar{4}3m$). The cryogenic electron energy loss spectroscopy (EELS) spectrum is also shown in Figure 3f, and its corresponding cryo-STEM image is provided in Figure S6. The strong peak at ∼20 eV and the broad shoulder signal at ∼38 eV originate from the Ge plasmon, and the broad signal at ∼29 eV corresponds to Ge

$M_{4,5}$ ionization, corroborating the existence of Ge in the particle of sol-LPGeSI.[48,49]

Finally, solution-processed $Li_{6.5}P_{0.5}Ge_{0.5}S_5I$ was applied for the infiltration of slurry-cast $LiCoO_2$ electrodes, as illustrated in Figure 4a. The $LiCoO_2$ electrodes used for the infiltration were fabricated by a conventional slurry-casting procedure with an electrode composition of 97:1:2 for $LiCoO_2$/polyvinylidenefluoride (PVDF)/super C65 by weight. As sulfide SEs have poor electrochemical oxidation stabilities and poor compatibility with layered oxide cathode materials, $LiCoO_2$ coated with $LiNbO_3$ was used.[4,50] A cross-sectional field-emission scanning electron microscopy (FESEM) image and its corresponding energy-dispersive X-ray spectroscopy (EDXS) elemental maps for the densified LPGeSI-infiltrated $LiCoO_2$ electrodes are shown in Figures 4b and S7. It is confirmed that LPGeSI makes intimate contact with $LiCoO_2$ with negligible void spaces. Electrochemical results for $LiCoO_2/Li_{0.5}In$ all-solid-state half-cells employing the LPGeSI-infiltrated $LiCoO_2$ electrodes cycled between 3.0 and 4.3 V (vs Li/Li⁺) at 30 °C are shown in Figure 4c−e. The first two-cycle charge−discharge voltage profiles at 0.1 C for all-solid-state cells with LPGeSI-infiltrated $LiCoO_2$ electrodes are shown, compared with conventional liquid electrolyte cells, in Figure 4c. The fraction of SE (LPGeSI) in the $LiCoO_2$ electrodes was as low as 12 wt %. The initial coulombic efficiency for the all-solid-state cells is lower (88.0%) than that for the liquid-electrolyte cells (94.5%), attributed to the irreversible electrochemical oxidation of sulfide SEs as indicated by the sloping voltage profile over 3 V (vs Li/Li⁺)
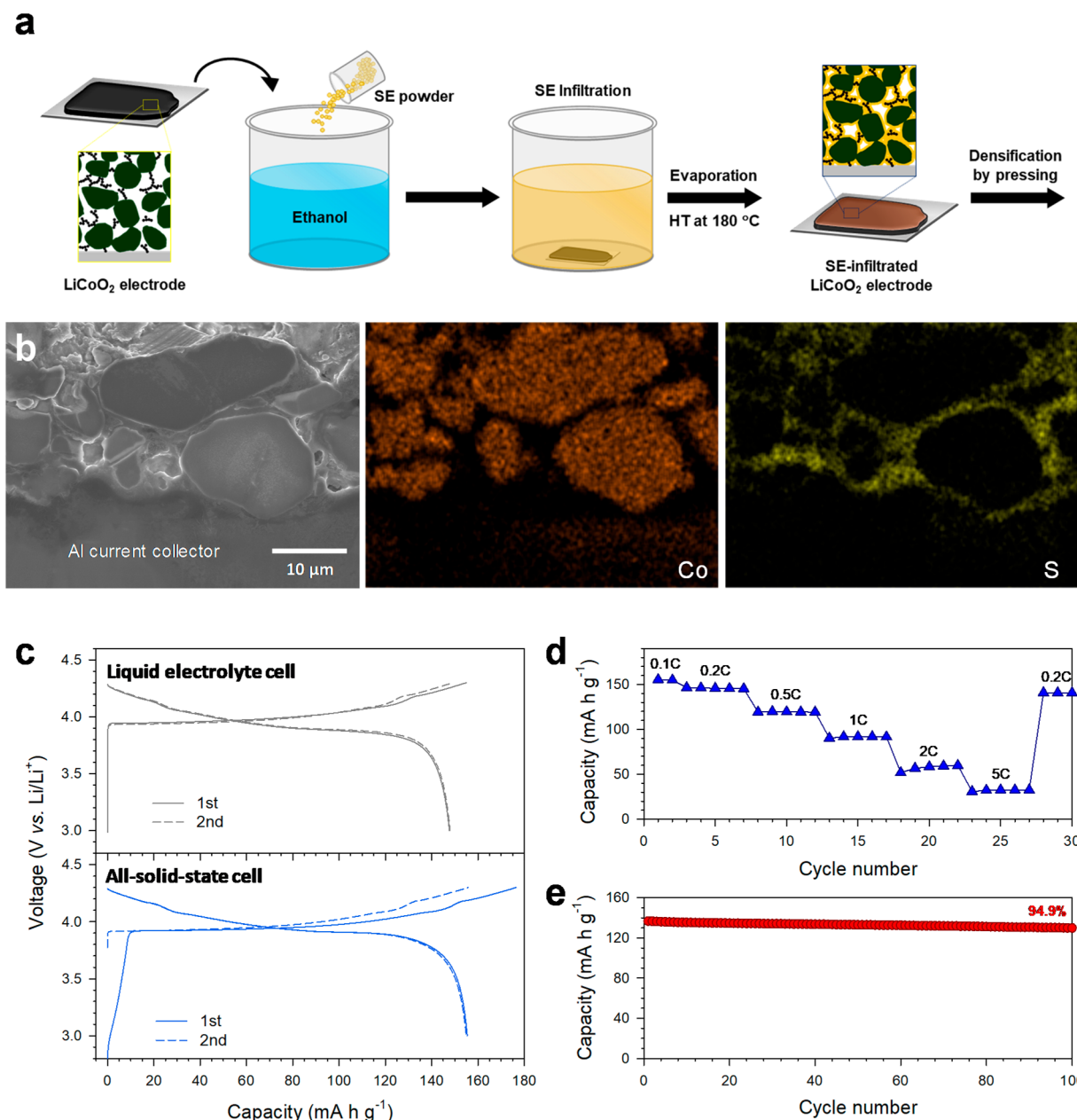
Figure 4. Electrochemical characterization of LiCoO$_2$/Li−In all-solid-state cells employing LPGeSI-infiltrated LiCoO$_2$ electrodes at 30 °C. (a) Schematic illustrating the infiltration of slurry-cast LiCoO$_2$ electrodes with LPGeSI−EtOH solutions. (b) Cross-sectional FESEM image of the LPGeSI-infiltrated LiCoO$_2$ electrodes and its corresponding EDXS elemental maps. (c) First two-cycle charge−discharge voltage profiles of LiCoO$_2$ electrodes at 0.1 C for liquid-electrolyte cells and all-solid-state cells. (d) Rate and (e) cycling performances at 0.2 C for the LPGeSI-infiltrated LiCoO$_2$ electrodes in all-solid-state cells.

during the first charge. Nevertheless, the LPGeSI-infiltrated LiCoO$_2$ electrodes exhibit no capacity loss (reversible capacity of 155 mA h g^{-1}) in comparison with the capacity of the liquid-electrolyte cells. As a control sample, LiCoO$_2$ electrodes prepared by the manual mixing of LiCoO$_2$, sol-LPGeSI, PVDF, and Super C65 were also prepared. The dry-mixture LiCoO$_2$ electrodes show much lower reversible capacity (109 mA h g^{-1}) and much larger interfacial resistance (230.2 Ω cm^2), as compared with the results of the LPGeSI-infiltrated LiCoO$_2$ electrodes (155 mA h g^{-1}, 26.0 Ω cm^2) (Figures S8−S10). These results clearly demonstrate the impacts of intimate ionic contacts and favorable ionic percolation enabled by the solution process.[22] The LPGeSI-infiltrated LiCoO$_2$ electrodes also show a decent rate capability (Figure 4d), highlighting the

impact of the high Li$^+$ conductivity of the solution-derived Li$_{6.5}$P$_{0.5}$Ge$_{0.5}$S$_5$I (0.54 mS cm^{-1}). Moreover, the capacity retention (Figure 4e) for LPGeSI-infiltrated LiCoO$_2$ electrodes cycled at 0.2 C after 100 cycles is as high as 94.9%, which is at the highest level in the all-solid-state battery field.[4,22,51]

In summary, we successfully developed highly Li$^+$-conductive solution-processable iodine-based Li argyrodites of LPSI, LPGeSI, and LPSnSI, with the highest Li$^+$ conductivity of 0.54 mS cm^{-1} at 30 °C for Li$_{6.5}$P$_{0.5}$Ge$_{0.5}$S$_5$I. The effect of composition and structure on Li$^+$ conductivity was investigated by complementary analysis using EIS, XRD, Raman spectroscopy, and PDF measurements. Importantly, the cryo-TEM measurement could successfully capture the local argyrodite nanocrystallites for sol-LPGeSI. We anticipate that the

fundamental findings from cryo-TEM will unveil the unknown areas that have been known as formidable challenges in sulfide electrolytes, such as the visualization of Li⁺ migration paths and electrochemically driven interfacial evolution.[41] Finally, excellent electrochemical performances of the LPGeSI-infiltrated LiCoO₂ electrodes for ASLBs operating at 30 °C were successfully demonstrated, highlighting the unique advantages of the intimate ionic contacts and the high Li⁺ conductivity for this solution-processable iodine-based Li argyrodites. We believe that our results provide important insights in understanding solid-state ionics in emerging low-crystalline materials (e.g., glass-ceramics, meta-materials) and the development of practical all-solid-state technologies to scale.

■ ASSOCIATED CONTENT

Ⓢ Supporting Information

The Supporting Information is available free of charge at https://pubs.acs.org/doi/10.1021/acs.nanolett.0c01028.

> Normal TEM video for a sol-LPGeSI sample showing the structural damage of sulfide solid electrolyte by an electron beam (MP4)

> Experimental methods, Raman spectra, Arrhenius plots of Li⁺ conductivity, cryogenic XRD pattern, cryo-TEM images, cross-sectional FESEM images and EDXS elemental maps, and electrochemical characterization for the manually mixed LiCoO₂ electrodes (PDF)

■ AUTHOR INFORMATION

Corresponding Authors

Hyun-Wook Lee — *School of Energy and Chemical Engineering, Department of Energy Engineering, Ulsan National Institute of Science and Technology (UNIST), Ulsan 44919, South Korea;* ⓘ orcid.org/0000-0001-9074-1619; Email: hyunwooklee@unist.ac.kr

Yoon Seok Jung — *Department of Energy Engineering, Hanyang University, Seoul 04763, South Korea;* ⓘ orcid.org/0000-0003-0357-9508; Email: yoonsjung@hanyang.ac.kr

Authors

Yong Bae Song — *Department of Energy Engineering, Hanyang University, Seoul 04763, South Korea*

Dong Hyeon Kim — *Department of Energy Engineering, Hanyang University, Seoul 04763, South Korea*

Hiram Kwak — *Department of Energy Engineering, Hanyang University, Seoul 04763, South Korea*

Daseul Han — *Department of Energy and Materials Engineering, Dongguk University, Seoul 04620, South Korea*

Sujin Kang — *School of Energy and Chemical Engineering, Department of Energy Engineering, Ulsan National Institute of Science and Technology (UNIST), Ulsan 44919, South Korea*

Jong Hoon Lee — *UNIST Central Research Facilities (UCRF), UNIST, Ulsan 44919, South Korea*

Seong-Min Bak — *Chemistry Division, Brookhaven National Laboratory, Upton, New York 11973, United States*

Kyung-Wan Nam — *Department of Energy and Materials Engineering, Dongguk University, Seoul 04620, South Korea;* ⓘ orcid.org/0000-0001-6278-6369

Complete contact information is available at:
https://pubs.acs.org/10.1021/acs.nanolett.0c01028

Notes

The authors declare no competing financial interest.

■ ABBREVIATIONS

LIB, lithium ion battery; SE, solid electrolyte; ASLB, all-solid-state Li or Li ion battery; EtOH, ethanol; TEM, transmission electron microscopy; cryo-TEM, cryogenic-TEM; EIS, electrochemical impedance spectroscopy; XRD, X-ray diffraction; PDF, pair distribution function; BM-LPMSI, ball-milled $Li_{6+x}P_{1-x}M_xS_5I$ (M = Ge, Sn); sol-LPMSI, solution-processed $Li_{6+x}P_{1-x}M_xS_5I$ (M = Ge, Sn); FFT, fast Fourier transform; SAED, selected-area electron diffraction; EELS, electron energy loss spectroscopy; PVDF, poly(vinylidene fluoride); FESEM, field-emission scanning electron microscopy; EDXS, energy-dispersive X-ray spectroscopy

■ REFERENCES

(1) Goodenough, J. B.; Kim, Y. Challenges for Rechargeable Li Batteries. *Chem. Mater.* **2010**, *22*, 587−603.

(2) Kato, Y.; Hori, S.; Saito, T.; Suzuki, K.; Hirayama, M.; Mitsui, A.; Yonemura, M.; Iba, H.; Kanno, R. High-power all-solid-state batteries using sulfide superionic conductors. *Nat. Energy* **2016**, *1*, 16030.

(3) Manthiram, A.; Yu, X.; Wang, S. Lithium battery chemistries enabled by solid-state electrolytes. *Nat. Rev. Mater.* **2017**, *2*, 16103.

(4) Park, K. H.; Bai, Q.; Kim, D. H.; Oh, D. Y.; Zhu, Y.; Mo, Y.; Jung, Y. S. Design Strategies, Practical Considerations, and New Solution Processes of Sulfide Solid Electrolytes for All-Solid-State Batteries. *Adv. Energy Mater.* **2018**, *8*, 1800035.

(5) Zhang, Z.; Shao, Y.; Lotsch, B.; Hu, Y.-S.; Li, H.; Janek, J.; Nazar, L. F.; Nan, C.-W.; Maier, J.; Armand, M.; Chen, L. New horizons for inorganic solid state ion conductors. *Energy Environ. Sci.* **2018**, *11*, 1945−1976.

(6) Li, M.; Wang, C.; Chen, Z.; Xu, K.; Lu, J. New Concepts in Electrolytes. *Chem. Rev.* **2020**, DOI: 10.1021/acs.chemrev.9b00531.

(7) Zhao, Q.; Stalin, S.; Zhao, C.-Z.; Archer, L. A. Designing solid-state electrolytes for safe, energy-dense batteries. *Nat. Rev. Mater.* **2020**, *5*, 229−252.

(8) Han, X.; Gong, Y.; Fu, K. K.; He, X.; Hitz, G. T.; Dai, J.; Pearse, A.; Liu, B.; Wang, H.; Rubloff, G.; Mo, Y.; Thangadurai, V.; Wachsman, E. D.; Hu, L. Negating interfacial impedance in garnet-based solid-state Li metal batteries. *Nat. Mater.* **2017**, *16*, 572−579.

(9) Zhou, L.; Assoud, A.; Zhang, Q.; Wu, X.; Nazar, L. F. A New Family of Argyrodite Thioantimonate Lithium Superionic Conductors. *J. Am. Chem. Soc.* **2019**, *141*, 19002−19013.

(10) Liu, Y.; Sun, Q.; Wang, D.; Adair, K.; Liang, J.; Sun, X. Development of the cold sintering process and its application in solid-state lithium batteries. *J. Power Sources* **2018**, *393*, 193−203.

(11) Deiseroth, H. J.; Kong, S. T.; Eckert, H.; Vannahme, J.; Reiner, C.; Zaiss, T.; Schlosser, M. Li$_6$PS$_5$X: a class of crystalline Li-rich solids with an unusually high Li$^+$ mobility. *Angew. Chem., Int. Ed.* **2008**, *47*, 755−758.

(12) Rayavarapu, P. R.; Sharma, N.; Peterson, V. K.; Adams, S. Variation in structure and Li$^+$-ion migration in argyrodite-type Li$_6$PS$_5$X (X = Cl, Br, I) solid electrolytes. *J. Solid State Electrochem.* **2012**, *16*, 1807−1813.

(13) de Klerk, N. J. J.; Rosłoń, I.; Wagemaker, M. Diffusion Mechanism of Li Argyrodite Solid Electrolytes for Li-Ion Batteries and Prediction of Optimized Halogen Doping: The Effect of Li Vacancies, Halogens, and Halogen Disorder. *Chem. Mater.* **2016**, *28*, 7955−7963.

(14) Kraft, M. A.; Culver, S. P.; Calderon, M.; Bocher, F.; Krauskopf, T.; Senyshyn, A.; Dietrich, C.; Zevalkink, A.; Janek, J.; Zeier, W. G. Influence of Lattice Polarizability on the Ionic Conductivity in the Lithium Superionic Argyrodites Li$_6$PS$_5$X (X = Cl, Br, I). *J. Am. Chem. Soc.* **2017**, *139*, 10909−10918.

(15) Kraft, M. A.; Ohno, S.; Zinkevich, T.; Koerver, R.; Culver, S. P.; Fuchs, T.; Senyshyn, A.; Indris, S.; Morgan, B. J.; Zeier, W. G. Inducing High Ionic Conductivity in the Lithium Superionic Argyrodites Li$_{6+x}$P$_{1-x}$Ge$_x$S$_5$I for All-Solid-State Batteries. *J. Am. Chem. Soc.* **2018**, *140*, 16330−16339.

(16) Boulineau, S.; Courty, M.; Tarascon, J.-M.; Viallet, V. Mechanochemical synthesis of Li-argyrodite Li$_6$PS$_5$X (X = Cl, Br, I) as sulfur-based solid electrolytes for all solid state batteries application. *Solid State Ionics* **2012**, *221*, 1−5.

(17) Zhou, L.; Park, K.-H.; Sun, X.; Lalère, F.; Adermann, T.; Hartmann, P.; Nazar, L. F. Solvent-Engineered Design of Argyrodite Li$_6$PS$_5$X (X = Cl, Br, I) Solid Electrolytes with High Ionic Conductivity. *ACS Energy Letters* **2019**, *4*, 265−270.

(18) Adeli, P.; Bazak, J. D.; Park, K. H.; Kochetkov, I.; Huq, A.; Goward, G. R.; Nazar, L. F. Boosting Solid-State Diffusivity and Conductivity in Lithium Superionic Argyrodites by Halide Substitution. *Angew. Chem., Int. Ed.* **2019**, *58*, 8681−8686.

(19) Ohno, S.; Helm, B.; Fuchs, T.; Dewald, G.; Kraft, M. A.; Culver, S. P.; Senyshyn, A.; Zeier, W. G. Further Evidence for Energy Landscape Flattening in the Superionic Argyrodites Li$_{6+x}$P$_{1-x}$M$_x$S$_5$I (M = Si, Ge, Sn). *Chem. Mater.* **2019**, *31*, 4936−4944.

(20) Miura, A.; Rosero-Navarro, N. C.; Sakuda, A.; Tadanaga, K.; Phuc, N. H. H.; Matsuda, A.; Machida, N.; Hayashi, A.; Tatsumisago, M. Liquid-phase syntheses of sulfide electrolytes for all-solid-state lithium battery. *Nat. Rev. Chem.* **2019**, *3*, 189−198.

(21) Yubuchi, S.; Teragawa, S.; Aso, K.; Tadanaga, K.; Hayashi, A.; Tatsumisago, M. Preparation of high lithium-ion conducting Li$_6$PS$_5$Cl solid electrolyte from ethanol solution for all-solid-state lithium batteries. *J. Power Sources* **2015**, *293*, 941−945.

(22) Kim, D. H.; Oh, D. Y.; Park, K. H.; Choi, Y. E.; Nam, Y. J.; Lee, H. A.; Lee, S. M.; Jung, Y. S. Infiltration of Solution-Processable Solid Electrolytes into Conventional Li-Ion-Battery Electrodes for All-Solid-State Li-Ion Batteries. *Nano Lett.* **2017**, *17*, 3013−3020.

(23) Yubuchi, S.; Uematsu, M.; Hotehama, C.; Sakuda, A.; Hayashi, A.; Tatsumisago, M. An argyrodite sulfide-based superionic conductor synthesized by a liquid-phase technique with tetrahydrofuran and ethanol. *J. Mater. Chem. A* **2019**, *7*, 558−566.

(24) Choi, Y. E.; Park, K. H.; Kim, D. H.; Oh, D. Y.; Kwak, H. R.; Lee, Y. G.; Jung, Y. S. Coatable Li$_4$SnS$_4$ Solid Electrolytes Prepared from Aqueous Solutions for All-Solid-State Lithium-Ion Batteries. *ChemSusChem* **2017**, *10*, 2605−2611.

(25) Park, K. H.; Oh, D. Y.; Choi, Y. E.; Nam, Y. J.; Han, L.; Kim, J. Y.; Xin, H.; Lin, F.; Oh, S. M.; Jung, Y. S. Solution-Processable Glass LiI-Li$_4$SnS$_4$ Superionic Conductors for All-Solid-State Li-Ion Batteries. *Adv. Mater.* **2016**, *28*, 1874−83.

(26) Banerjee, A.; Park, K. H.; Heo, J. W.; Nam, Y. J.; Moon, C. K.; Oh, S. M.; Hong, S. T.; Jung, Y. S. Na$_3$SbS$_4$: A Solution Processable Sodium Superionic Conductor for All-Solid-State Sodium-Ion Batteries. *Angew. Chem., Int. Ed.* **2016**, *55*, 9634−8.

(27) Heo, J. W.; Banerjee, A.; Park, K. H.; Jung, Y. S.; Hong, S.-T. New Na-Ion Solid Electrolytes Na$_{4-x}$Sn$_{1-x}$Sb$_x$S$_4$ (0.02 ≤ x ≤ 0.33) for All-Solid-State Na-Ion Batteries. *Adv. Energy Mater.* **2018**, *8*, 1702716.

(28) Kim, D. H.; Lee, H. A.; Song, Y. B.; Park, J. W.; Lee, S.-M.; Jung, Y. S. Sheet-type Li$_6$PS$_5$Cl-infiltrated Si anodes fabricated by solution process for all-solid-state lithium-ion batteries. *J. Power Sources* **2019**, *426*, 143−150.

(29) Duchêne, L.; Kim, D. H.; Song, Y. B.; Jun, S.; Moury, R.; Remhof, A.; Hagemann, H.; Jung, Y. S.; Battaglia, C. Crystallization of closo-borate electrolytes from solution enabling infiltration into slurry-casted porous electrodes for all-solid-state batteries. *Energy Storage Mater.* **2020**, *26*, 543−549.

(30) Kim, D. H.; Lee, Y.-H.; Song, Y. B.; Kwak, H.; Lee, S.-Y.; Jung, Y. S. Thin and Flexible Solid Electrolyte Membranes with Ultrahigh Thermal Stability Derived from Solution-Processable Li Argyrodites for All-Solid-State Li-Ion Batteries. *ACS Energy Lett.* **2020**, *5*, 718−727.

(31) Liu, Z.; Fu, W.; Payzant, E. A.; Yu, X.; Wu, Z.; Dudney, N. J.; Kiggans, J.; Hong, K.; Rondinone, A. J.; Liang, C. Anomalous high ionic conductivity of nanoporous beta-Li$_3$PS$_4$. *J. Am. Chem. Soc.* **2013**, *135*, 975−978.

(32) Ito, S.; Nakakita, M.; Aihara, Y.; Uehara, T.; Machida, N. A synthesis of crystalline Li$_7$P$_3$S$_{11}$ solid electrolyte from 1, 2-dimethoxy-ethane solvent. *J. Power Sources* **2014**, *271*, 342−345.

(33) Han, F.; Yue, J.; Zhu, X.; Wang, C. Suppressing Li Dendrite Formation in Li$_2$S-P$_2$S$_5$ Solid Electrolyte by LiI Incorporation. *Adv. Energy Mater.* **2018**, *8*, 1703644.

(34) Lim, H. D.; Lim, H. K.; Xing, X.; Lee, B. S.; Liu, H.; Coaty, C.; Kim, H.; Liu, P. Solid electrolyte layers by solution deposition. *Adv. Mater. Interfaces* **2018**, *5*, 1701328.

(35) Cengiz, M.; Oh, H.; Lee, S.-H. Lithium Dendrite Growth Suppression and Ionic Conductivity of Li$_2$S-P$_2$S$_5$-P$_2$O$_5$ Glass Solid Electrolytes Prepared by Mechanical Milling. *J. Electrochem. Soc.* **2019**, *166*, A3997−A4004.

(36) Hao, F.; Chi, X.; Liang, Y.; Zhang, Y.; Xu, R.; Guo, H.; Terlier, T.; Dong, H.; Zhao, K.; Lou, J.; Yao, Y. Taming Active Material-Solid Electrolyte Interfaces with Organic Cathode for All-Solid-State Batteries. *Joule* **2019**, *3*, 1349−1359.

(37) Yubuchi, S.; Tsukasaki, H.; Sakuda, A.; Mori, S.; Hayashi, A.; Tatsumisago, M. Quantitative analysis of crystallinity in an argyrodite sulfide-based solid electrolyte synthesized via solution processing. *RSC Adv.* **2019**, *9*, 14465−14471.

(38) Dietrich, C.; Weber, D. A.; Sedlmaier, S. J.; Indris, S.; Culver, S. P.; Walter, D.; Janek, J.; Zeier, W. G. Lithium ion conductivity in Li$_2$S-P$_2$S$_5$ glasses - building units and local structure evolution during the crystallization of superionic conductors Li$_3$PS$_4$, Li$_7$P$_3$S$_{11}$ and Li$_4$P$_2$S$_7$. *J. Mater. Chem. A* **2017**, *5*, 18111−18119.

(39) Park, K. H.; Kim, D. H.; Kwak, H.; Jung, S. H.; Lee, H.-J.; Banerjee, A.; Lee, J. H.; Jung, Y. S. Solution-derived glass-ceramic NaI·Na$_3$SbS$_4$ superionic conductors for all-solid-state Na-ion batteries. *J. Mater. Chem. A* **2018**, *6*, 17192−17200.

(40) Liao, M.; Cao, E.; Julius, D.; Cheng, Y. Structure of the TRPV1 ion channel determined by electron cryo-microscopy. *Nature* **2013**, *504*, 107−112.

(41) Li, Y.; Li, Y.; Pei, A.; Yan, K.; Sun, Y.; Wu, C.-L.; Joubert, L.-M.; Chin, R.; Koh, A. L.; Yu, Y.; Perrino, J.; Butz, B.; Chu, S.; Cui, Y. Atomic structure of sensitive battery materials and interfaces revealed by cryo-electron microscopy. *Science* **2017**, *358*, 506.

(42) Wang, J.; Huang, W.; Pei, A.; Li, Y.; Shi, F.; Yu, X.; Cui, Y. Improving cyclability of Li metal batteries at elevated temperatures and its origin revealed by cryo-electron microscopy. *Nat. Energy* **2019**, *4*, 664−670.

(43) Wang, X.; Li, Y.; Meng, Y. S. Cryogenic Electron Microscopy for Characterizing and Diagnosing Batteries. *Joule* **2018**, *2*, 2225−2234.

(44) Ferrari, A. C. Raman spectroscopy of graphene and graphite: Disorder, electron-phonon coupling, doping and nonadiabatic effects. *Solid State Commun.* **2007**, *143*, 47−57.

(45) Gouadec, G.; Colomban, P. Raman Spectroscopy of nanomaterials: How spectra relate to disorder, particle size and mechanical properties. *Prog. Cryst. Growth Charact. Mater.* **2007**, *53*, 1−56.

(46) Schlem, R.; Muy, S.; Prinz, N.; Banik, A.; Shao-Horn, Y.; Zobel, M.; Zeier, W. G. Mechanochemical Synthesis: A Tool to Tune Cation Site Disorder and Ionic Transport Properties of Li_3MCl_6 (M = Y, Er) Superionic Conductors. *Adv. Energy Mater.* **2020**, *10*, 1903719.

(47) Yubuchi, S.; Uematsu, M.; Deguchi, M.; Hayashi, A.; Tatsumisago, M. Lithium-Ion-Conducting Argyrodite-Type Li_6PS_5X (X = Cl, Br, I) Solid Electrolytes Prepared by a Liquid-Phase Technique Using Ethanol as a Solvent. *ACS Appl. Energy Mater.* **2018**, *1*, 3622−3629.

(48) Pantel, R.; Cheynet, M. C.; Tichelaar, F. D. Comparison of Si and Ge low-loss spectra to interpret the Ge contrast in EFTEM images of $Si_{1-x}Ge_x$ nanostructures. *Micron* **2006**, *37*, 657−665.

(49) Tripathi, M.; Markevich, A.; Bottger, R.; Facsko, S.; Besley, E.; Kotakoski, J.; Susi, T. Implanting Germanium into Graphene. *ACS Nano* **2018**, *12*, 4641−4647.

(50) Jung, S. H.; Oh, K.; Nam, Y. J.; Oh, D. Y.; Brüner, P.; Kang, K.; Jung, Y. S. Li_3BO_3-Li_2CO_3: Rationally Designed Buffering Phase for Sulfide All-Solid-State Li-Ion Batteries. *Chem. Mater.* **2018**, *30*, 8190−8200.

(51) Jung, S. H.; Kim, U. H.; Kim, J. H.; Jun, S.; Yoon, C. S.; Jung, Y. S.; Sun, Y. K. Ni-Rich Layered Cathode Materials with Electrochemo-Mechanically Compliant Microstructures for All-Solid-State Li Batteries. *Adv. Energy Mater.* **2020**, *10*, 1903360.